AIAA JOURNAL
Vol. 47, No. 11, November 2009

Assessment of Computational Fluid Dynamics for Supersonic Shock Containing Jets

Steven A. E. Miller,* Jérémy Veltin,* Philip J. Morris,† and Dennis K. McLaughlin‡
Pennsylvania State University, University Park, Pennsylvania 16802

DOI: 10.2514/1.44336

This paper describes a combined experimental and computational investigation of supersonic jets operating off design. Axisymmetric steady-state computational fluid dynamics simulations were performed with a Reynolds-averaged Navier–Stokes solver using a two-equation turbulence model. These results were compared directly with experimental results for two differen t axisymmetric nozzles operating at over- and underexpanded conditions. Pitot and static pressure probes were used to measure the Mach number and local static pressure at various downstream locations. A comparison of both experimental and numerically predicted schlieren visualizations were performed for a qualitative assessment of the accuracy of the flowfield predictions. Quantitative comparisons of pitot and static pressures were made between the experiments and simulations. This provides an assessment of the quality of the numerical simulations as well as an indication of the errors associated with any interference between the pressure probes and the flow in the experiments.

Nomenclature

a_∞	=	ambient speed of sound
a_j	=	speed of sound at nozzle exit
D	=	diameter of nozzle exit
D_p	=	diameter of static pressure probe
k	=	turbulent kinetic energy
M_d	=	design Mach number of nozzle
M_j	=	fully expanded jet Mach number
M_1	=	local Mach number
P_p	=	local pitot pressure
P_{to}	=	total pressure in the plenum
P_{t1}	=	local total pressure
P_{t2}	=	local total pressure behind a normal shock
P_1	=	local static pressure
P_∞	=	atmospheric pressure
T_o	=	jet stagnation temperature
T_∞	=	atmospheric temperature
U_j	=	mean exhaust velocity
x	=	downstream direction, coordinate
x_h	=	location of static pressure ports
y	=	cross-stream direction, coordinate
y^+	=	coordinate in viscous wall layer
z	=	observer direction, coordinate
β	=	nozzle off-design parameter
γ	=	ratio of specific heats
ρ	=	local density

Introduction

THIS paper describes a combination of experimental and computational study of supersonic jets operating off design. The motivations for the work are twofold. First, the results of the numerical simulations form the basis for a prediction model of Broadband shock-associated noise (BBSAN) presently under development by the authors. This model requires a knowledge of the time-averaged velocity field, the pressure perturbations associated with the shock cell structure, as well as information about the turbulence length and time scales, which can be obtained if a two-equation turbulence model is used. Second, it is known that the presence of pitot and static pressure probes in the turbulent flow may interfere with the natural development of the jet. Once confidence has been established in the numerical simulations, they can be used to indicate locations in which experimental measurement are less reliable and the reasons for this decrease in accuracy.

A series of pitot and static pressure probe measurements have been conducted and compared with CFD simulations at various downstream and cross-stream locations. Quantitative comparisons are made with profiles and contour plots of the local Mach number M_1 and local static pressure P_1. Schlieren images of the jets are compared with density gradients calculated from the numerical simulation database. Finally, the calculated database is used to predict profiles and contours of a local stagnation pressure behind a local normal shock wave. This quantity P_{t2} can be compared directly with the experimental pitot pressure as additional evidence of the quality of the computations. The measurements are performed for two imperfectly expanded jets issuing from two different nozzles: a converging nozzle with a design Mach number M_d of 1.0 operating at a fully expanded Mach number M_j of 1.5, and a converging–diverging nozzle with $M_d = 1.5$ and $M_j = 1.3$. The nozzle pressure ratios (NPR) for these two jet conditions are $P_{to}/P_\infty = 3.67$ and 2.77, respectively. The total temperature ratio for both jets is $T_o/T_\infty = 1.00$. Both nozzles are axisymmetric, and axisymmetric CFD simulations are conducted to obtain solutions to the time-averaged equations of motion. Such steady calculations require significantly less computational time compared with time dependent calculations that have been used in the past for direct calculations of the flow and radiated noise. This provides the potential for relatively rapid predictions of BBSAN once the noise prediction models are fully implemented.

BBSAN is one of two components of shock-associated noise found in supersonic jets operating off-design. The other is screech, which is often not a concern in aircraft engines due to their geometry and high temperature ratios. There have been two moderately successful BBSAN models developed to date. Harper-Bourne and Fisher [1] proposed a theoretical model which regarded each shock/shear layer interaction as a source of acoustic radiation. In the basic model, each source is equally spaced. In their experiments, they

Presented as Paper 2988 at the 14th AIAA/CEAS Aeroacoustics Conference, Vancouver, BC, Canada, 5–7 May 2008; received 12 March 2009; revision received 24 July 2009; accepted for publication 24 July 2009.

*Graduate Research Assistant, Department of Aerospace Engineering, 233 Hammond Building. Member AIAA.
†Boeing/A. D. Welliver Professor, Department of Aerospace Engineering, 233 Hammond Building. Fellow AIAA.
‡Professor, Department of Aerospace Engineering, 233 Hammond Building. Fellow AIAA.

isolated the shock-associated noise, and proposed the β^4 law. The shock noise intensity, given by Harper-Bourne and Fisher, scales with β^4 where, β is the off-design parameter defined as:

$$\beta = \sqrt{|M_j^2 - M_d^2|} \tag{1}$$

It should be noted that the Harper-Bourne and Fisher model was developed for $M_d = 1$ only.

Tam [2] developed a stochastic model for BBSAN based on the interaction between the large-scale structures in the jet shear layer and shock cell structure. The model of the turbulence in the jet is a random superposition of instability waves. The noise is calculated as a sum of the noise contributions from different interaction modes. Each mode is generated by the interaction of the large-scale turbulent structures, modeled as traveling waves, with the quasi-periodic shock cell structure, modeled using a Fourier–series representation. Only those frequency/wave number components of the interaction that have a sonic phase velocity in the direction of a far-field observer can radiate.

Both of these models for BBSAN, as well as that under development by the authors, argue that the noise generation mechanism is associated with the interaction of the jet shear layer turbulence with the quasi-periodic shock cell structure in the jet. Thus the accurate simulation of the development of the jet flow is a key component of any noise prediction model.

The remainder of this section describes the analysis method for the experimental data and an overview of the numerical simulations. The next section describes the experimental facility and details of the Reynolds-averaged Navier–Stokes (RANS) simulations. The procedures used for processing both the experimental and computational data are also described. This is followed by comparisons of the experimental measurements and numerical simulations. Finally, some conclusions are drawn and plans for future research are summarized.

Experimental Background

Static and pitot pressure measurements were made in the jet flow. The schematic diagrams presented in Fig. 1 show the nomenclature used for the pressures measured by the probes. When a flow is supersonic, the total pressure after the shock P_{t2} and the static pressure P_1 are related to the Mach number in the flow M_1 by the Rayleigh–Pitot formula:

$$\frac{P_{t2}}{P_1} = \left[\frac{(\gamma+1)}{2}M_1^2\right]^{\frac{\gamma}{\gamma-1}}\left[\frac{\gamma+1}{2\gamma M_1^2-(\gamma-1)}\right]^{\frac{1}{\gamma-1}} \tag{2}$$

The measured pitot pressure P_p is then equal to the total pressure P_{t2}. In the mixing layer, in which the Mach number falls below unity, the isentropic formula should be applied locally:

$$\frac{P_p}{P_1} = \left[1+\frac{(\gamma-1)}{2}M_1^2\right]^{\frac{\gamma}{\gamma-1}} \tag{3}$$

To obtain a good representation of the value of the static pressure in the flow in the absence of the static probe, it has been shown [3] that the distance between the static pressure ports and the tip of the probe, $x_k - x$, should be at least 10 times the diameter D_p of the static probe.

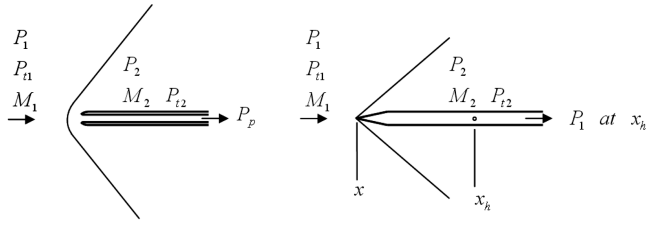

a) b)

Fig. 1 Schematic of a pressure probe in a freestream flow: a) pitot probe, and b) static pressure probe.

Then the static pressure P_1 measured by the probe is a good representation of the static pressure in the flow at location x_k in the absence of any probe (provided the probe is aligned with the local oncoming flow). The use of any smaller value of $x_k - x$ leads to a measured static pressure lower than the actual value. In the present experiments, $x_k - x$ is 12.7 mm and D_p is 1 mm.

If the flow direction is known, knowledge of three appropriate gas dynamic properties in a compressible flow is sufficient to uniquely specify all the properties of the flow. In an adiabatic flow of this type the isoenergetic approximation of constant jet stagnation temperature, T_o, is very accurate. Across the mixing layer, the static temperature can also be accurately estimated using the Crocco relation. There are two viable options for the two remaining required quantities that can be measured or estimated. First, the static pressure can be combined with the pitot pressure to compute the local Mach number using Eq. (2) or Eq. (3) depending on the local Mach number. Second, an alternate method can be used when a reasonable estimate of P_{t1} can be made. This is the case for the converging nozzle condition in the isentropic flow region within the shear layer and upstream of the first oblique shock waves. In this region the normal shock relation for P_{t2}/P_{t1} is

$$\frac{P_{t2}}{P_{t1}} = \left[\frac{(\gamma+1)M_1^2}{(\gamma-1)M_1^2+2}\right]^{\frac{\gamma}{(\gamma-1)}}\left[\frac{\gamma+1}{2\gamma M_1^2-(\gamma-1)}\right]^{\frac{1}{(\gamma-1)}} \tag{4}$$

and can be used (implicitly) to compute the Mach number. This method is used in the present paper in regions in which the static pressure probe measurements have inaccuracies and will be discussed further as the processed data are presented.

Numerical Background

The RANS-CFD simulations are conducted using the Wind-US code [4]. Wind-US is a product of the National Project for Application-Oriented Research in CFD (NPARC) Alliance, a partnership between the NASA John H.Glenn Research Center at Lewis Field and the U.S. Air Force Arnold Engineering Development Center. The code has been extensively tested and numerous validation cases (for simple flows) have been established. In relation to the present research, the code has been used to predict the development of single- and dual-stream supersonic jets for both axisymmetric and nonaxisymmetric cases. Georgiadis and Papamoschou [5] and Franko and Georgiadis [6] performed simulations of heated, high-speed, dual-stream jets. Georgiadis and Papamoschou [7] also simulated flow in dual-stream jets with an eccentric core flow. Recently, Georgiadis et al. [8] have performed an evaluation of different two-equation turbulence models for heated jet flows. This last study is of particular importance to the present validation as it provides an assessment of the quality of two-equation turbulence models for both unheated and heated jet flows. It was found that some models, such as the Tam–Ganesan [9] k-ε formulation, improved the mean flow predictions. All models tested gave similar predictions for the turbulent kinetic energy. The k-ε model of Chien [10] and the shear stress transport (SST) k-ω model of Menter [11] are standard two-equation turbulence models implemented in Wind-US. The Menter SST turbulence model uses the traditional k-ω model of Wilcox [12] in the inner region of the boundary layer. In the outer region of the boundary layer the Menter SST turbulence model automatically switches to a k-ε format. The models definition of eddy viscosity better accounts for the effects of transport of turbulent shear stress. In free shear flows the Menter SST model acts like a k-ε model. The present simulations with Wind-US provide the mean velocity field, including the shock cell structure, as well as values of either k-ε or k-ω, depending on which of the two turbulence models is chosen.

Methods

The previous section of the paper described the various experimental and numerical methods used to generate results for the two selected nozzles. In this section, the experimental facility and methods used to obtain the time-averaged quantities as well as the

setup for schlieren visualization are first described. The CFD, grid generation, and the boundary conditions implemented for the axisymmetric simulations with Wind-US are then outlined. The turbulence model and numerical schemes to solve the equations are also discussed. Finally, a description is given of the methods used to transform the experimental and numerical data into the plots produced in the results section.

Experimental Setup

The experiments were conducted in the high-speed jet noise facility at Pennsylvania State University. This facility uses a Kaeser air compressor to pressurize two 18.9 m^3 tanks to a pressure of 1.34 MPa (195 psig). This compressed air passes through a dryer and is then piped to a plenum before exhausting through a model nozzle. Control of the flow is achieved with pressure regulators and valves whereas a total pressure sensor in the plenum is used to monitor the flow produced at the nozzle exit. Nozzle diameters up to 25.4 mm are typically used, even though the experiments presented in this paper focus on 12.7 mm-diam nozzles. Because this facility is primarily used for acoustic and optical measurements, the jets exhaust into an anechoic chamber. More information on the capabilities and specifications of this facility can be found in Doty and McLaughlin [13].

The pitot and static pressure probes used for the pressure measurements are shown in Fig. 2. Because of the range in which they operate and to optimize the resolution of the data, different pressure transducers are used for each probe. The pitot probe uses a 100 psi Setra transducer whereas the static pressure probe uses a 20 psi Validyne transducer. Both measurements are performed in a very similar way, using a set of two Velmex motorized slides connected onto a Velmex VXM controller that is in turn operated by a personal computer running LabVIEW software. The voltage from the pressure transducer is acquired at 10 Hz for 3 s at each location using a PCI-6110 National Instruments' data acquisition board card and is stored for postprocessing.

Measurements were made every $0.2D$ in the downstream direction, and every $0.02D$ in the vertical direction, through half of the jet, starting at $0.8D$ below the jet axis (giving 41 points). Static pressure probe measurements were made only in the radial range from the centerline to $0.4D$ (providing 21 points) for axial positions less than one jet diameter. This range limitation is due to the nozzle lip obstructing probe movement. The data were later mirrored along the centerline to give a full picture of the jet.

In addition to the pressure probe measurements, schlieren images of the flow were recorded with and without the probes using a conventional Z-type schlieren system described in detail in Veltin and McLaughlin [14]. It provides a qualitative image of the flow as well as helping to locate the probes in the flow and assessing the effects of the probes on the flow pattern.

Axisymmetric RANS Simulations

The CFD solutions were produced by the NPARC Wind-US 2.0 code. Wind-US solves the Euler or Navier-Stokes equations numerically with support for chemically reacting flows and turbulence models. It has the capability to perform these calculations on structured and unstructured grids in two or three dimensions. There are a large number of numerical schemes included which allow for the solution of both steady and unsteady fluid dynamic problems. Wind-US has been shown to be robust and a large number of validation tests of the code have been completed. A number of helpful pre- and postprocessing utilities are provided with Wind-US to support the user in creating and interpreting problems.

The Wind-US solver finds RANS solutions using nondimensional forms of the equations, however, the input to the Wind-US solver must use dimensional quantities. These quantities are restricted to the use of English units. Once the simulation is complete, these values are again nondimensionalized based on the plenum pressure for experimental comparison. Second-order Roe upwind flux splitting is used for spatial discretization and an implicit time marching scheme is used to integrate the solution. The flowfields are integrated in time until a steady solution is achieved. This combination of numerical algorithms are default for Wind-US; however, other techniques are available that may better model the shock waves of the shock cell structure.

The boundary conditions for the solution of the problem consist of an inflow boundary at the entrance of the nozzle. At this location, stagnation temperature and pressure are specified to match the experimental conditions and velocities are set normal to the inlet plane. These inlet velocity vectors are parallel to the streamwise direction. These values correspond to the pressure in the plenum P_{to} and the ambient temperature T_∞. An inviscid wall boundary condition is constructed on the axis of symmetry of the nozzle. This boundary condition, in addition to the axisymmetric command in the Wind-US input file, runs the simulation in axisymmetric mode. The downstream exit of the domain uses a general outflow boundary condition which only requires a pressure specification. In the present simulations, the downstream pressure boundary condition is set as the freestream pressure P_∞. Other flowfield values are extrapolated from interior points of the domain to the outlet boundary using zeroth order extrapolation. The wall of the nozzle, including its lip and external surface, are set as no-slip adiabatic viscous walls. Finally, the boundary conditions in the far field are set as freestream boundary conditions with a Mach number of 0.001 as well as with atmospheric temperature and pressure. A small value of Mach number must be specified for proper stability of the simulation. Figure 3 shows the layout of the boundary conditions for the numerical simulations. The flow moves from left to right. The profile of the nozzle can be seen in the lower left hand corner. The extent of the domain downstream from the nozzle exit is 75 nozzle diameters. The range of the computational domain in the cross-stream direction is 50 nozzle diameters.

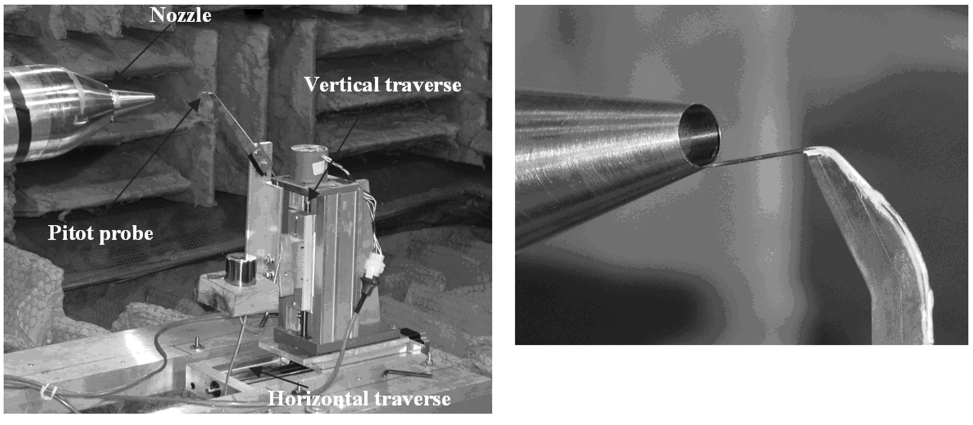

a) b)

Fig. 2 Experimental setup: a) pitot probe and traverses, and b) static pressure probe at the lip of the nozzle.

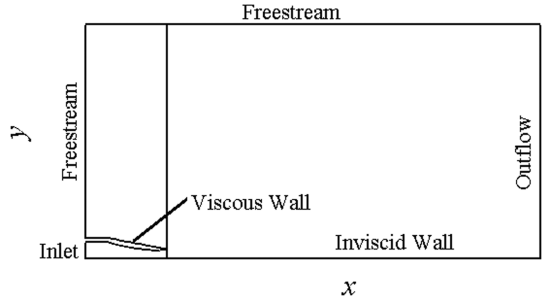

Fig. 3 Layout of the computational domain for the axisymmetric Wind-US simulation. The boundary conditions are shown at the respective boundaries. There are three blocks in each axisymmetric simulation. Note that the domain is not to scale.

The nozzle coordinates available for numerically modeling the convergent section of the nozzle do not extend very far upstream relative to the divergent section. The convergent section of the nozzle is created as far upstream from the throat as possible, from the available geometry of the nozzles. The wall of the nozzle is extended three to four diameters in the upstream direction and parallel to the centerline axis. This extension of the nozzle inlet in the upstream direction uses inviscid wall boundary conditions. The extended region is created in part for stability of the inlet boundary condition.

Computational grids for Wind-US are created with the software program Gridgen. The coordinates of the nozzle are imported into Gridgen from a list of points in a text file as a database. The internal wall, external wall, and nozzle lip are generated by creating connectors along the database coordinates. The region in which the jet flow is formed corresponds to the large area in Fig. 3 on the right. An additional region is added before this region in the freestream above the nozzle's outside surface. This is the second largest region of the computational grid. Finally, a third region of the computational domain represents the inside of the nozzle. Because two different nozzles are considered in the present study, two corresponding computational grids were created in 2-D. Figure 4 illustrates the contours of the nozzles with the grid and also a closer view of the grid near the nozzle exit. Regions of high grid density include the throat of the nozzle, the exit of the nozzle, the shear layer region, and the jet centerline. Grid density is higher in these regions to ensure that the flow is well resolved in these important regions. The local wall-shear stress at the nozzle exit is estimated from an equivalent flow speed and downstream distance of a flat-plate turbulent boundary layer. By setting y^+ to one, the distance to the first grid point is calculated using this estimated wall-shear stress and kinematic viscosity. The grid is stretched for computational efficiency using the default hyperbolic tangent function built into Gridgen. Initial grid point distances at the wall and exit lines of the grid are set by specifying the distance in inches. The total number of grid points for the converging and converging–diverging cases are 759,609 and 485,323 points, respectively. There are a larger number of grid points in the converging case because it was used originally to generate results at larger values of x/D than needed in the present study. The number of grid points is very high for axisymmetric calculations because these solutions were used in integration independence studies of RANS-based noise prediction methods. Computational grid-independence studies are conducted by comparing the solutions obtained by skipping every other grid point in each indices direction. A slightly less refined grid is also generated for the converging–diverging nozzle with grid points that do not coincide with those of the original grid. These less refined solutions indicate that the solutions generated by the prescribed numerical methods are grid-independent.

Simulations were run until both convergence is achieved and a visual inspection of the solution yields satisfactory results. Convergence is achieved when the global residual remains constant with increasing iterations of the solution. Grid sequencing was used in both cases to speed up convergence. Sequencing in Wind-US means systematically skipping grid points in the i-, j-, or k-indices directions of a structured computational grid. This essentially generates a coarsened grid for the initial iterations. For initial solutions, grid sequencing every fourth grid point in every indices direction was used until convergence is achieved. Thereafter, the solution from the sequenced grid was interpolated onto every grid point. Wind-US is restarted using the coarse solution using no grid sequencing until convergence is achieved in the entire domain, thereby finding the solution on every grid point. Both cases used approximately 120,000 iterations until convergence. The simulations were run in serial mode because the benefit from parallelism would be small due to the relatively low number of grid points. This would not be the case for fully 3-D simulations. A parallel version of the code is available and has been tested but it has not been used in the present study. There are a number of choices of turbulence models to close the RANS equations available in Wind-US including algebraic, one-, and two-equation models. There are three two-equation models available, however, for its ease of use, the Menter k-ω turbulence model was selected for all the following numerical simulations. Furthermore, two-equation models are needed for the noise models being developed by the authors.

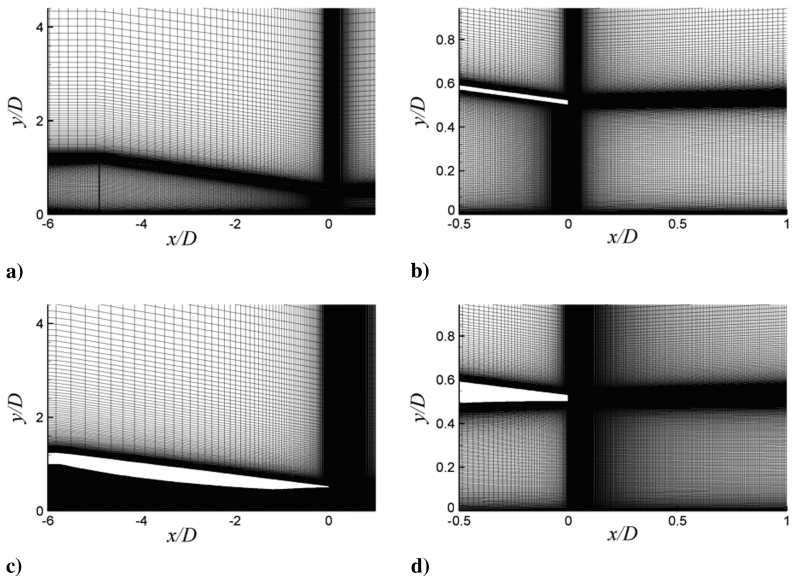

Fig. 4 Nozzle profiles and closeup of grid at the nozzle exit plane: a) contour of the converging nozzle, b) closeup of the nozzle exit of the converging nozzle, c) contour of the converging–diverging nozzle, and d) closeup of the nozzle exit of the converging–diverging nozzle.

Data Processing Methods

The data acquired during the pressure probe measurements were first inspected for inconsistent values. Averaging of all the points acquired at each spatial location was then performed before application of the pressure transducer calibration curves. The resulting pressures were nondimensionalized with P_{to}, mirrored around the jet axis, transformed into a matrix, and finally exported for plotting. Wherever both the static and pitot pressure are measured with a high level of reliability, they are directly used to compute the local Mach number. In regions in which the Mach number is above unity, Eq. (2) is used, where, P_{t2} and P_1 are measured with the pitot and static probes, respectively. Within the shear layer, in which the local Mach number drops below unity as already mentioned in the Experimental Background section, the isentropic relations of Eq. (3) can be directly used to compute M_1. At locations in which the static pressure measurements have inaccuracies (discussed in the results section), the Mach number is computed through Eq. (4) from the measured pitot pressure and by making an estimate of the total pressure in the jet. These estimates take into account the fact that the flow may have negotiated a number of oblique shock waves and are corrected accordingly. Finally, it should be noted that most of these equations are solved implicitly using a MATLAB routine.

In preparation for comparisons, the variables determined from the experiments also need to be extracted from the Wind-US solutions. This was performed by using the Wind-US utility CFPOST, which reads the output files from Wind-US and has a number of postprocessing abilities. Using CFPOST, the output files from Wind-US are read and converted into Plot3d format. The Plot3d files contain the quantities ρ, M_1, P_1, and P_{to}. Because cross-stream gridlines in the jet flow correspond to each x/D location, these lines are extracted and put into a separate database. All the variables and corresponding grids are in dimensional form. These are then normalized by the nozzle exit diameter, D and the plenum pressure P_{to}.

Numerical schlieren are produced by taking the derivative of the local density ρ in the cross-stream direction y using the Tecplot CFD analysis package. The data, which is axisymmetric, is mirrored on the x axis so that a copy is placed below the computed data. This allows for plotting of contours across the x axis. The sign of the gradient of density below the x axis is then changed. This is done to simulate the inversion of the light gradients observed in the experiments.

Experimental and Numerical Simulation Comparisons

As a first qualitative comparison between the experimental and numerical results, comparisons of the general nature of the flowfield were made. These involve taking a schlieren image of the experimental flows using both the converging and converging–diverging nozzles and comparing them side by side, with the numerical schlierens. The numerical contours of $\partial\rho/\partial y$ are plotted over a very small range of negative one to one with 100 intervals. This is done to emphasize the smallest features of the density gradients and to magnify any possible imperfections in the numerical simulation. The converging nozzle case is shown in Fig. 5a. The top image in the figure represents the experimental results and the bottom image shows the numerical results. The axes of the figures, along with the subsequent figures in this paper, are nondimensionalized by the diameter of the nozzle D. The flow is from left to right in the positive x-axis direction. The lips of the nozzle at $y/D = \pm 0.5$ are evident by the shear layer spreading from these locations. The sharp demarcation between dark and light regions emanating from the nozzle lip and ending on the jet centerline indicates the end of the Prandtl–Meyer expansion fan and the initiation of compression waves caused by the interaction of the expansion waves with the free shear layer. Additionally, the shock waves and their corresponding angles can be seen as strong gradients of $\partial\rho/\partial y$. The first conical oblique shock originates at the same location in both experiment and simulations at approximately $x/D = 1.1$. The second oblique shock wave occurs at approximately $x/D = 2.5$. In both these figures the origin of these shock waves is the same. By inspection of this figure, the angles of both the experimental and numerical oblique shock waves agree. This shows that the calculated and experimental shock wave strengths are equal. However, a slight discrepancy occurs at approximately $x/D = 1.1$, at the center of the jet. The experimental visualization shows a very short normal shock, before the oblique shock waves. This normal shock creates a small subsonic region downstream, delimited by slip lines. Any increase in the NPR shows a broadening of this subsonic region. The numerical results only start showing this phenomenon when the simulated NPR is increased slightly to produce a fully expanded Mach number $M_j = 1.53$.

Figure 5b shows a comparison between the experimental and numerical schlierens for the converging–diverging nozzle case. The arrangements of the shocks are very different because, unlike the converging nozzle case, an oblique shock wave originates at the nozzle lip and terminates as a barrel shock. The appearance of the more typical conical oblique shocks downstream ensues. A qualitative comparison of the position and angles of the shock waves shows good agreement. In particular, the normal shock just downstream of the exit of the nozzle is in the same position. The slip stream downstream of the normal shock is also seen clearly in the simulations.

A more quantitative analysis is appropriate to evaluate the accuracy of the averaged variables of the RANS solution compared with experimental results. The calculation of these data was discussed in the preceding section on Data Processing Methods. As noted in that section, there are some choices made in the combination of equations to be used to evaluate the flow parameters (such as the local Mach number). In these choices, the pitot pressure is always used. For this reason the simulation data are manipulated to produce profiles of local stagnation pressure at a point that would be measured directly behind a hypothetical pitot probe. This manipulation involves using the Mach number and local static pressure ahead of the hypothetical shock that would be formed in the presence of a probe. Figure 6 shows profiles of these calculated data compared with the pressure measured by the pitot probe (normalized with the plenum pressure). For reference, the nozzle exit is at $x/D = 0.0$ and

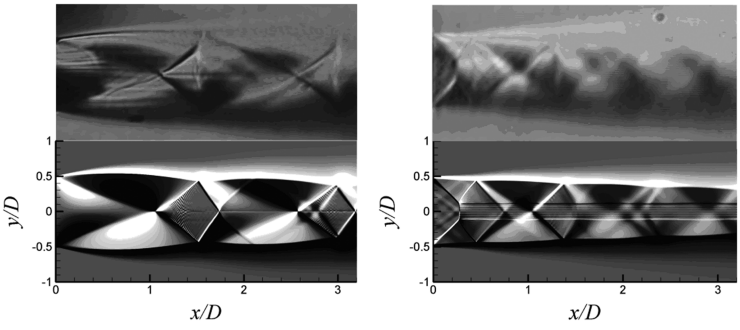

Fig. 5 Comparison between the experimental and numerical schlieren: a) the converging nozzle case $M_d = 1.0, M_j = 1.5$; b) the converging–diverging nozzle case $M_d = 1.5, M_j = 1.3$. The nozzle exit is at $x/D = 0.0$ and the flow moves from $x/D = 0.0$ to the positive direction. The nozzle centerline is at $y/D = 0.0$ and the nozzle lips at $y/D = \pm 0.5$.

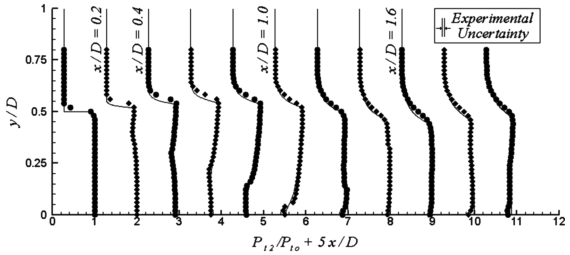

Fig. 6 Comparison between the experimental (dots) and numerical (lines) P_{t2}/P_{to} of the $M_d = 1.0, M_j = 1.5$ converging nozzle case. Each set of data is separated by $x/D = 0.20$ starting at $x/D = 0.0$ at the left and stopping at $x/D = 2.0$ on the right.

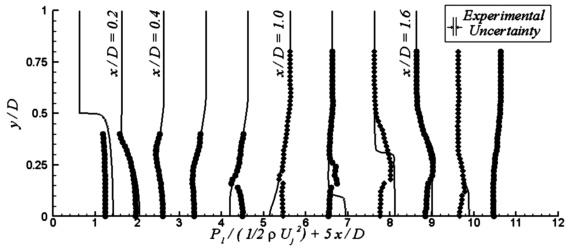

Fig. 7 Comparison between the experimental (dots) and numerical (lines) $P_1/(1/2\rho U_j^2)$ of the $M_d = 1.0$, $M_j = 1.5$ converging nozzle case. Each set of data is separated by $x/D = 0.20$ starting at $x/D = 0.0$ at the left and stopping at $x/D = 0.20$ on the right.

the nozzle lip is at $x/D = 0.0$ and $y/D = 0.5$. An uncertainty estimate of the measurement is shown graphically on the figure. This uncertainty, approximately 4% of the mid range value of pitot pressure, is predominantly due to the variance of the transducer output voltage from the linear fit to the calibration. The repeatability with which the pitot pressure measures the centerline stagnation pressure for subsonic jets (operating with no shock waves) is included in the final uncertainty estimate of the measurement. The comparisons of experimental and computed results show excellent agreement at all x/D locations. The shear layer experimental data shows a small shift in the positive y direction that is a result of slight initial probe misalignment with the jet lip line.

Figure 7 shows a comparison of P_1/P_{to} data for the converging nozzle case. The uncertainty estimate shown graphically on the figure is approximately 6% of the mid range static pressure measurement, but does not include errors caused by the distortion of the flow in a nonuniform flowfield. Such an effect is evident in specific regions of the flow including the region near which the oblique shock wave originates at approximately $x/D = 1.0$. The data in this region near the centerline of the jet show larger differences between the experimental and numerical solutions (larger than the pressure transducer uncertainty). It is likely that the discrepancies observed can be attributed to the interaction of the flow within the oblique shock created by the tip of the probe with other flow gradients (such as the mixing layer or the jet shock waves) that reflects back to the probe body upstream of the static pressure hole. This can produce an error difficult to predict due to the complex shape of the mixing layer and the three dimensionality of the problem.

The schlieren image of Fig. 8a shows the static pressure probe before its traversing the jet. The round circle along the probe's body represents the location of the pressure tap. Figure 8b offers a good visualization of the static pressure probe and shock wave interactions. In this figure, one can clearly see the shock wave created at the tip of the probe being reflected on the shear layer (at point A) and subsequently impinging on the static pressure tap. On the other hand, the presence of the probe also produces a large disturbance of the shock cell geometry when located closer to the center of the jet, as can be seen when comparing Figs. 8a, 8c, and 8d. The shock cell pattern naturally occurring in a jet running under these conditions has been consequently altered once the probe is close to the jet axis. In addition to the shock attached at the tip of the probe seen in Fig. 8c, one can also notice a shockwave appearing along the body of the probe (at point B) that is very similar to what would be observed in a transonic flow. Although all these modifications in the flow pattern would not influence pitot probe measurements, which are obtained at the tip of the probe, it does effect the results from a static probe because the holes for pressure measurements are located downstream of the tip of the probe. Therefore, to produce more reliable predictions of Mach number and velocities, the static pressure measurement data are not used when they diverge from the numerical predictions. Rather, Eq. (4) is used, with the assumption that $P_{t1} = P_{to}$ within the shear layer and upstream of the first oblique shock waves. Downstream of the first shock and in the center of the jet, there is a small subsonic region, bounded by slip lines and observed in Fig. 5a. In this region, the isentropic relation of Eq. (3) is used to compute the Mach number, therefore, requiring the use of the measured values of P_1.

Figure 9 shows the local Mach number, M_1, calculated as seen earlier and presented at the same locations as the previous figures. Some discrepancies appear near the jet centerline starting at $x/D = 1.2$ due to the presence of the normal shock observed in the experiment but not in the numerical predictions. Some discrepancies are also apparent in the outer part of the mixing layer, in which the experimental results exhibit a less smooth appearance than along the rest of the traverses. At these locations, the computed velocities are

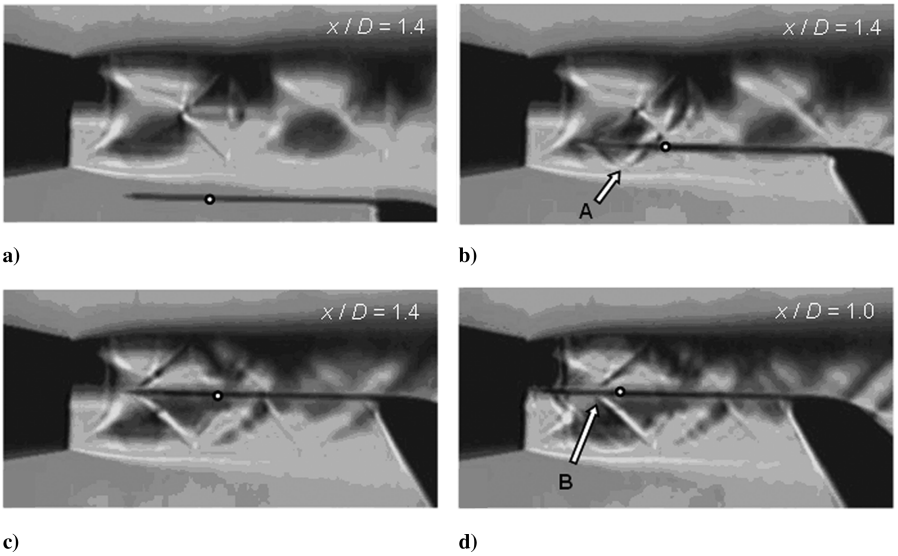

Fig. 8 Schlieren images of static pressure probe in a $M_d = 1.0$, and $M_j = 1.5$ jet: a–c) probe at $x/D = 1.4$, d) probe at $x/D = 1.0$; and $D = 0.5$ in.

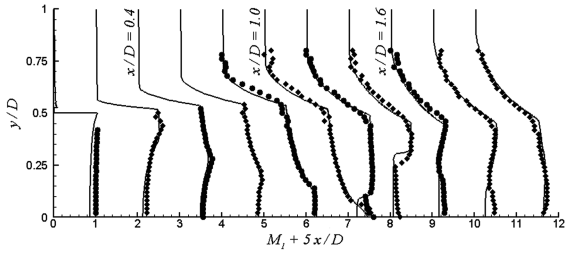

Fig. 9 Comparison between the experimental (dots) and numerical (lines) M_1 of the $M_d = 1.0$, $M_j = 1.5$ converging nozzle case. Each set of data is separated by $x/D = 0.20$ starting at $x/D = 0.0$ at the left and stopping at $x/D = 0.20$ on the right.

very low. These local speeds correspond to very low pressure values measured by the pitot probe pressure transducers. As discussed earlier, the uncertainties are estimated at 4 and 6% of the mid range value, respectively, for the static and the pitot pressure. Therefore, these low speed measurements are below the precision achievable with the current setup.

An additional problem appears near the nozzle exit in which the static pressure probe cannot traverse to the nozzle lip line in which it would encounter the nozzle. Therefore, the M_1 experimental plot at $x/D = 0.0$ shows a smaller radial range than its numerical counterpart. Furthermore, the numerical results at this location show that the velocity is zero on the nozzle lip; this accounts for the large gradient in the region near $y/D = 0.5$ compared with the experimental data. The spreading rate of the jet, shown by the lower gradients of pressure in the shear layer, is consistent with the numerical results for the range of x/D measured.

The results of the pitot probe traverses for the converging–diverging nozzle case are shown in Fig. 10. These experimental pitot pressure profiles show good overall agreement with the calculations for a hypothetical probe from the numerical simulations. By inspection of Fig. 10, the predicted growth rate of the shear layer is lower than the experimental data. The Menter SST turbulence model behaves like a k-ε turbulence model in free shear flows. Thus, the deficiencies inherent in k-ε turbulence models for free shear flows are also apparent in the results of the Menter SST model. The Menter SST model was not designed for supersonic off-design jets and is operating outside its range of calibration. There currently exists no steady RANS-based turbulence model that correctly predicts the field variables of a supersonic off-design jet. Figure 11 shows the corresponding static pressure measurements. Note that the static pressure has been nondimensionalized with respect to $\rho U_j^2/2$ for a clearer representation. These also have good agreement. However, as in the convergent nozzle case, there is one small disagreement in the static pressure data. This is at approximately $x/D = 0.2$, which is the region of the bottom of the barrel shock, seen in the schlieren image in Fig. 5b. The discrepancy is probably due to reasons similar to those that can be observed from the schlieren images of Fig. 8 and discussed in the previous section.

The final profile comparison, of the local Mach number in the converging–diverging case, is shown in Fig. 12. These Mach number estimates use the data from the static pressure probe with the Rayleigh–pitot formula Eq. (2) and (3) to produce quite good agreement between experiment and computations. However, the error due to the static pressure probe interaction with the barrel shock at $x/D = 0.2$ is apparent. The static pressure measurement has altered the solution for the Mach number at this point.

Additionally, Fig. 13 shows the centerline values of M_1 for both the over- and underexpanded jets obtained only from the numerical simulations. The variations of M_1 are in visual agreement with the schlieren images of Fig. 5. The semiperiodic spacing of the centerline Mach number of the overexpanded jet is lower than the underexpanded jet as the overexpanded case is operating more off design. It should also be noted that the mean Mach number values are in close agreement with the theoretical M_j values derived from the prescribed pressure ratio.

Overall there is quite good agreement between the numerical and experimental results for the measured averaged flow quantities. In some cases, particularly the converging nozzle profiles, it appears that the data are shifted by a very small amount in the y direction. This small apparent shift, without which the results would agree even better, is due to the relatively large probe size compared with the exit diameter of the nozzle. The exit diameter of both nozzles is only 12.7 mm and the diameters of the pitot and the static pressure probe are 0.51 and 0.96 mm, respectively. The relatively large diameter compared with the diameter of the nozzle and fluid dynamic structures is probably the cause of this small shift. An example of this shift can be seen in Fig. 6, in which the very sharp shear layer at the nozzle exit does not align with the sharp shear layer of the numerical results. However, this error is relatively small and the remaining agreement is excellent.

In the case of some of the data, the results of numerical predictions can be compared well on contour plots. An example is a contour plot of the pitot pressure for the converging nozzle jet operating at a pressure ratio that produces a mean Mach number of 1.5. The top part of Fig. 14, above the x axis, represents the axisymmetric numerical prediction. The contours below the x axis are generated with experimental data. The 100 contour levels, shown in the upper portion of the figures, range from zero to one. In regions in which

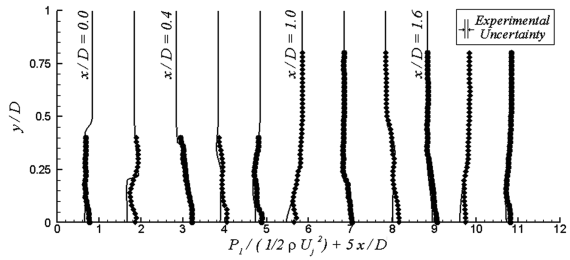

Fig. 11 Comparison between the experimental (dots) and numerical (lines) $P_1/(1/2\rho U_j^2)$ of the $M_d = 1.5$, $M_j = 1.3$ converging–diverging nozzle case. Each set of data is separated by $x/D = 0.20$ starting at $x/D = 0.0$ at the left and stopping at $x/D = 2.0$ on the right.

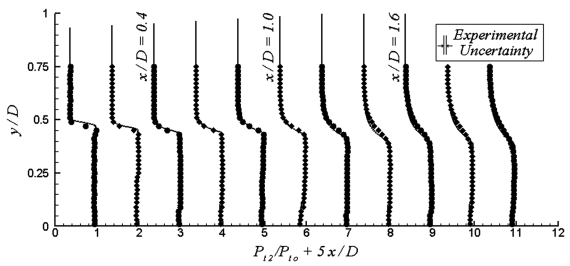

Fig. 10 Comparison between the experimental (dots) and numerical (lines) P_{t2}/P_{to} of the $M_d = 1.5$, $M_j = 1.3$ converging–diverging nozzle case. Each set of data is separated by $x/D = 0.20$ starting at $x/D = 0.0$ at the left and stopping at $x/D = 2.0$ on the right.

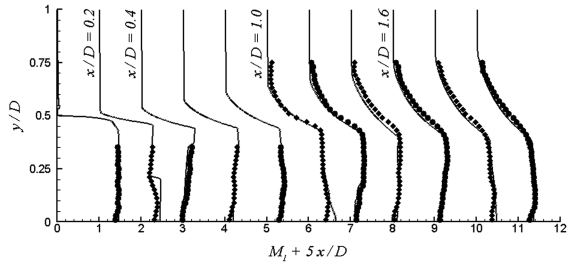

Fig. 12 Comparison between the experimental (dots) and numerical (lines) M_1 of the $M_d = 1.5$, $M_j = 1.3$ converging–diverging nozzle case. Each set of data is separated by $x/D = 0.20$ starting at $x/D = 0.0$ at the left and stopping at $x/D = 2.0$ on the right.

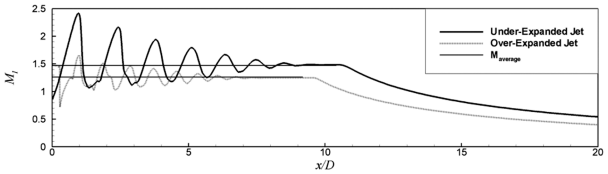

Fig. 13 Centerline Mach number for the jets operating at $M_d = 1.0$, $M_j = 1.5$, and $M_d = 1.5$, $M_j = 1.3$. The average Mach number is shown for both jets in the core.

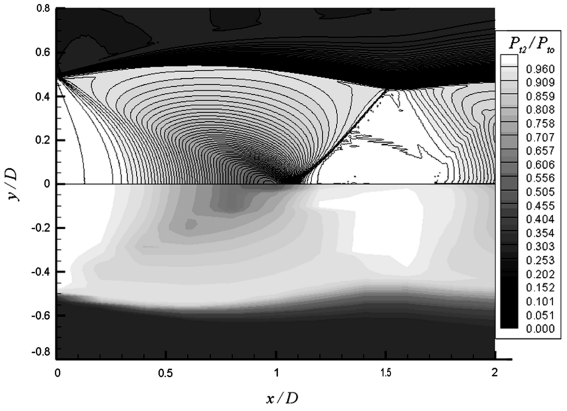

Fig. 14 Contour plot comparison between the experimental (bottom) and numerical (top) P_{t2}/P_{to} of the $M_d = 1.0$, $M_j = 1.5$ converging nozzle case.

there are not large gradients of total pressure, the qualitative agreement between the two plots is very good. However, in regions in which shocks occur, the contour plots of the experimental data are smeared. This is due to the lack of resolution of the experimental data in terms of axial spacing between experimental data points. Clearly, it is impractical to perform experimental measurements at every computational grid location. The largest separation between experimental data points is $0.2D$ which is the spacing between probe measurements in the x direction. This resolution limitation did not affect the good agreement in the shear layer growth in the measured region. However, a place in which the lack of resolution is apparent is near the oblique shocks, which are extremely thin.

Four contour plots have been constructed entirely from the numerical simulations data of the static pressure and Mach number for both cases. These are shown in Fig. 15. All the contour plots have 100 contour levels. For the static pressure the range is from 0.0 to 1.0 and for the Mach number the range is from 0.0 to 2.5. The shock waves are very well defined by the clustering of the contours and the shock cell structure is apparent. Figure 15 is able to capture the slip stream caused by the barrel shock in this converging–diverging case. This change in Mach number due to the normal shock is not apparent in the schlieren in Fig. 5 because it is relatively small in magnitude.

Conclusions

Pitot and static pressure probe measurements have been made in two supersonic jets operating at off-design pressure ratios. One converging nozzle (design Mach number of 1.0) is operating at a fully expanded Mach number of 1.5. The second case is a converging–diverging nozzle with a design Mach number of 1.5 operating at a fully expanded Mach number of 1.3. The experimental and computational comparisons agree very well at most positions for both cases examined. Only when the pressure probe data are being used in which the shock waves are highly focused (along the jet axis) are there discrepancies in the comparisons. However, the pitot pressure measurements agree closely with those calculated from the simulated data for all cases. The static pressure measurements show small differences with the calculated values because of the shock wave interactions with the probe. When the Mach number is calculated from the pitot and static pressures, the small errors in static pressure effect the Mach number.

Future experimental efforts include the operation of larger jets to improve the probe resolution. Following that, both experiments and simulations will include nonaxisymmetric (rectangular) jets and heated jet conditions simulated with helium-air gas mixtures. Experiments with these jets are already underway. The CFD results produced for axisymmetric simulations and 3-D simulations will be used as input for the BBSAN prediction methodology presently under development.

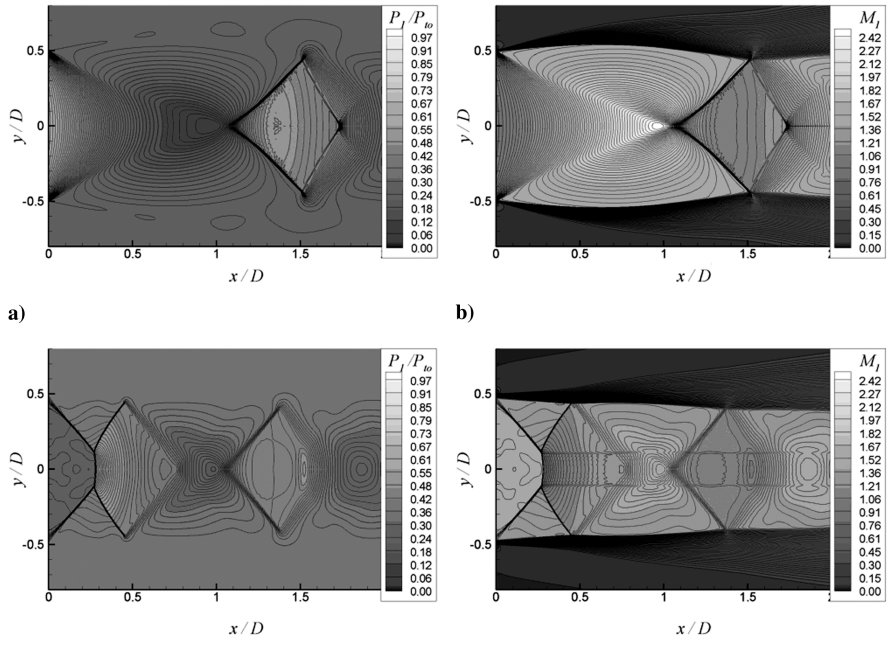

Fig. 15 Various contour plots of the two CFD simulations: a) $M_d = 1.0$, $M_j = 1.5$, contours of P_1/P_{to}; b) $M_d = 1.0$, $M_j = 1.5$ contours of M_1; c) $M_d = 1.5$, $M_j = 1.3$, contours of P_1/P_{to}; and d) $M_d = 1.5$, $M_j = 1.3$, contours of M_1.

Acknowledgments

This research is sponsored by the NASA Cooperative Agreement NNX07AC88A entitled, "A Comprehensive Model for the Prediction of Supersonic Jet Noise." The Technical Monitor is Milo Dahl. The authors would like to express their gratitude to Nick Georgiadis of the NASA John H. Glenn Research Center at Lewis Field for his helpful advice with Wind-US. Ujas Patel is acknowledged for helping develop the Labview data acquisition code and for additional help conducting the experiments.

References

[1] Harper-Bourne, M., and Fisher, M. J., "The Noise from Shock-Waves in Supersonic Jets," AGARDograph, CP-131, 1973, pp. 1–13.

[2] Tam, C. K. W., "Stochastic Model Theory of Broadband Shock Associated Noise from Supersonic Jets," *Journal of Sound and Vibration*, Vol. 116, No. 2, 1987, pp. 265–302.

[3] Liepman, H. W., Roshko, A., and Dhawan, S., "On Reflection of Shock Waves from Boundary Layers," NACA, Rept. 1100, 1952.

[4] Nelson, C., and Power, G., "The NPARC Alliance Flow Simulation System," AIAA, Paper 2001-0594, 2001.

[5] Georgiadis, N. J., and Papamoschou, D., "Computational Investigations of High-Speed Dual-Stream Jets," AIAA, Paper 2003-3311, 2003.

[6] Franko, K. J., and Georgiadis, N. J., "Computational Investigation of Heated High-Speed Coaxial Jets," AIAA Paper 2004-2980, 2004.

[7] Georgiadis, N. J., and Papamoschou, D., "Computations of Dual-Stream Jets with Eccentric and Coaxial Bypass Streams," AIAA Paper 2004-2981.

[8] Georgiadis, N. J., Yoder, D. A., and Engblom, W. B., "Evaluation of Modified Two-Equation Turbulence Models for Jet Flow Predictions," *AIAA Journal*, Vol. 44, No. 12, pp. 3107–3114. doi:10.2514/1.22650

[9] Tam, C. K. W., and Ganesan, A., "Modified k-ε Turbulence Model for Calculating Hot Jet Mean Flows and Noise," *AIAA Journal*, Vol. 42, No. 1, 2004, pp. 26–34. doi:10.2514/1.9027

[10] Chien, K.-Y., "Predictions of Channel and Boundary-Layer Flows with a Low Reynolds Number Turbulence Model," *AIAA Journal*, Vol. 20, No. 1, Jan. 1982, pp. 33–38. doi:10.2514/3.51043

[11] Menter, F. R., "Two-Equation Eddy-Viscosity Turbulence Models for Engineering Applications," *AIAA Journal*, Vol. 32, No. 8, Aug. 1994, pp. 1598–1605. doi:10.2514/3.12149

[12] Wilcox, D. C., "Reassessment of the Scale-Determining Equation for Advanced Turbulence Models," *AIAA Journal*, Vol. 26, No. 11, 1988, pp. 1299–1310. doi:10.2514/3.10041

[13] Doty, M. J., and McLaughlin, D. K., "Acoustic and Mean Flow Measurements of High-Speed, Helium/Air Mixture Jets," *International Journal of Aeroacoustics*, Vol. 2, No 3, July 2003, pp. 293–334. doi:10.1260/147547203322986151

[14] Veltin, J., and McLaughlin, D. K., "Noise Mechanisms Investigation in Shock Containing Screeching Jets Using Optical Deflectometry," AIAA Paper 2008-2889, May 2008.

C. Bailly
Associate Editor